Classifying Human Brain Tumors by Lipid Imaging with Mass Spectrometry

Livia S. Eberlin[1], **Isaiah Norton**[2], **Allison L. Dill**[1], **Alexandra J. Golby**[2], **Keith L. Ligon**[3], **Sandro Santagata**[3], **R. Graham Cooks**[1,*], and **Nathalie Y.R. Agar**[2,*]

[1]Department of Chemistry and Center for Analytical Instrumentation Development, Purdue University, West Lafayette, IN 47907 (USA)

[2]Department of Neurosurgery, Department of Radiology, and Department of Medical Oncology, Brigham and Women's Hospital and Dana-Farber Cancer Institute, Harvard Medical School, Boston, MA 02115 (USA)

[3]Department of Pathology, Brigham and Women's Hospital, Harvard Medical School, Boston, MA 02115 (USA)

Abstract

Brain tissue biopsies are required to histologically diagnose brain tumors, but current approaches are limited by tissue characterization at the time of surgery. Emerging technologies such as mass spectrometry imaging can enable a rapid direct analysis of cancerous tissue based on molecular composition. Here we illustrate how gliomas can be rapidly classified by desorption electrospray mass spectrometry (DESI-MS) imaging, multivariate statistical analysis, and machine learning. DESI-MS imaging was performed on thirty-six human glioma samples, including oligodendroglioma, astrocytoma and oligoastrocytoma, all of different histologic grades and varied tumor cell concentration. Grey and white matter from glial tumors were readily discriminated and detailed diagnostic information could be provided. Classifiers for subtype, grade and concentration features generated with lipidomic data showed high recognition capability with >97% cross-validation. Specimen classification in an independent validation set agreed with expert histopathology diagnosis for 81% of tested features. Together, our findings offer proof of concept that intra-operative examination and classification of brain tissue by mass spectrometry can provide surgeons, pathologists, and oncologists with critical and previously unavailable information to rapidly guide surgical resections that can improve management of patients with malignant brain tumors.

Keywords

classification of human gliomas; lipid profiles; mass spectrometry imaging; neurosurgery; ambient mass spectrometry

---

*Corresponding authors: **Professor R. Graham Cooks**, Department of Chemistry, Purdue University, West Lafayette, IN, 47907, Tel: (+1) 765-494-5262, Fax: (+1) 765-494-9421, cooks@purdue.edu, **Dr. Nathalie Y. R. Agar**, Department of Neurosurgery, Brigham and Women's Hospital, Harvard Medical School, Boston, MA 02115, Tel: (+1) 617-525-7374, Fax: (+1) 617-264-6316, nagar@bwh.harvard.edu.

Conflict of Interest: No conflicts of interested are disclosed.

Introduction

Critical decisions in medicine often depend upon discriminating normal from diseased tissue. For over a century, one of the central methods for identifying pathological processes has been the microscopic review of tissue sections by the trained eye of human pathologists. This paradigm has been simple yet powerful and has allowed for tremendous advances in the understanding, classification and treatment of many human diseases. Over the last few decades newer modalities have been developed to further enhance the capabilities of microscopy-based tissue diagnosis, particularly for the evaluation of tumors. These tests however remaining largely non-quantitative, require days or even weeks to complete and often assess very specific questions rather than provide comprehensive analytical information. New modalities could further empower the practice of surgical pathology, and assist in defining the extent of a tumor (1), and its relationship to surrounding non-neoplastic tissue (2-5). Such new modalities will need to be applicable in real-time, and be validated using standard histopathology evaluation.

Among the most useful ancillary tests in molecular pathology are those that detect changes in nucleic acids that are at the foundation of tumorigenesis: DNA point mutations and chromosomal translocations (6, 7). Proteomic information is also used regularly in pathology, albeit in a low throughput manner using immunohistochemistry. Mass spectrometry imaging methods have been increasingly applied to cancer research due to its ability of being able to simultaneously map the distribution of large populations of proteins, a feature that is potentially of enormous diagnostic and prognostic value (8). The lipid constituents of tissues, however, remain entirely unused in diagnostic practice. Extensive investigations have established that the lipid composition of tissues can vary with disease state (9). A number of studies focus on the molecular changes that occur in cells, signaling the beginning of malignancy and providing a means for early detection and treatment intervention (10, 11). These lipidomic findings emphasize the importance of determining the composition of lipids in biological tissues for its diagnostic and prognostic value. Despite the diverse lipid composition of various tissues, lipidomic information has until recently been impractical to acquire. Desorption electrospray ionization-mass spectrometry (DESI-MS) and related MS imaging methods have now made acquisition of information on specific lipids and their distribution in tissue highly practical.

DESI-MS is one of a recently developed group of ionization techniques in MS in which samples are examined in the ambient environment with minimal pretreatment (12, 13), therefore potentially applicable to real-time analyses. Using DESI, direct lipid analysis from biological samples such as tissue sections can be performed rapidly and routinely (14). Chemical information obtained can be represented as two-dimensional images recording abundances and spatial distributions of specific ions (15). In a single analysis, DESI-MS allows the characterization and imaging of many lipids including fatty acyls, glycerophospholipids, glycerolipids and sphingolipids(14). DESI-MS imaging experiments have been conducted on human cancerous tissues including bladder (16), kidney (17), prostate (18) and testicular (19) cancers. In a pilot study using a limited number of specimens, DESI-MS imaging enabled discrimination of different WHO grades of astrocytomas based on lipid profiles (20).

While imaging of individual ions can be used to distinguish tumor from normal tissue, in most diseases the use of multiple ions enhances diagnostic classification and creates diagnostic categories that often cannot be discerned by examination of single ion data or by the visual examination of broad range mass spectral data. Here, we report on the use of multivariate statistical approaches to provide correlation between lipidomic data acquired by DESI MS imaging and glioma diagnostic information such as subtype, grade, and

concentration. A robust classification method was developed, validating the use of lipid profiles for the near real-time characterization of complex gliomas.

Material and Methods

Tissue samples

All tissue samples were cerebrum tumor tissue obtained from the BWH Neurooncology Program Biorepository collection, and analyzed under approved Institutional Review Board (IRB) protocol, with informed written consent obtained by licensed neurosurgeons at BWH. Sample list is shown in Table S1. Samples were flash frozen and stored in liquid nitrogen and stored at −80°C until sectioned at 14 μm thickness using a Microm HM550 cryostat (Mikron Instruments Inc., San Marcos, CA), and thaw mounted onto glass slides. The slides were stored in closed containers at −80° C; prior to analysis they were allowed to come to room temperature, and dried under in a dessicator for approximately 15 minutes.

DESI-MS analysis

The DESI ion source was a lab-built prototype (15), similar to a commercial source from Prosolia Inc. (Indianapolis, IN USA). DESI-MS experiments were carried out in the negative and in the positive ion mode. For more details, see Supporting Data. The tissues were scanned using a 2D moving stage in horizontal rows separated by a 200 μm vertical step. An in-house program allowed the conversion of the XCalibur 2.0 mass spectra files (.raw) into a format compatible with the Biomap software (21) with which spatially accurate images were assembled. Lipid species were tentatively identified based on collision-induced dissociation experiments (CID) tandem MS experiments and comparison with literature data. DESI imaging of all tissue samples were run in a randomized way using the same experimental conditions. Samples were obtained in three different sets, and each set included specimens of different subtypes and grades. Each set was run in a random sequence, and under the same experimental conditions. Replicate data were recorded.

Histopathology analysis

H&E stained serial tissue sections were optically scanned using Mirax Micro 4SL telepathology system from Zeiss (Jena, Germany). Regions of heterogeneity within tissue sections were digitally assigned by the pathologist and compared to DESI-MS ion images. Tumor content was evaluated by two neuropathologists (S.S. and K.L.) through examination of an H&E stained tissue section, which was adjacent to the one used for DESI-MS imaging studies. Specimens were evaluated and scored visually with respect to their percentage of tumor nuclei relative to the total nuclei in the sample. Samples were also characterized and assigned a qualitative from normal to infiltrative to solid, corresponding from low to high cellularity.

Statistical Analysis

Samples were divided into training and validation sets for statistical analysis. Each class was defined with similar numbers of specimens, and only specimens with clear diagnosis in accordance with the WHO classification system (22) were used (agreement between two neuropathologists). A software tool was developed to enable the selection of regions of interest (ROI) based on visual inspection of the DESI ion image loaded in Biomap. More specifically, a rectangle with x,y coordinates is drawn over an ion image to create a ROI, and the corresponding spectral data is extracted from the ROI, saved in a separate folder, and converted for further analysis using ClinProTools 2.2 (Bruker Daltonics). The entire mass spectrum acquired, from m/z 200 to m/z 1000, was imported into ClinProTools and used for classification. ROIs were selected to be constituted of approximately 100 spectra

each, so that each specimen weighs somewhat equivalently in a classification model, and to avoid including background signal from the glass. For heterogeneous cases, ROIs were selected based on neuropathological evaluation and demarcation of ROIs within the tissue section, as visualized on the optical image of the H&E stained adjacent section. All ROIs were assigned by the neuropathologist for tumor subtype, grade and cell concentration.

Three distinct classifiers were built to recognize glioma subtype, grade, and tumor cell concentration. Classification models were built with the Support Vector Machine algorithm. For each classifier, the number of input peaks was automatically detected based on clustering of the peak rankings as determined by the SVM hyperplane separation with an upper limit of 25 peaks to be used by the classifier.

The calculated models were used to classify spectra from selected sub-regions for each validation sample. After classification, the class membership was reported by ClinProTools for every spectrum file with corresponding (x,y) spatial coordinates. To create the overlay image, corresponding H&E-stained optical image, ion image, and class image were imported into an image composition program (23), and manually aligned using rotation and scaling transforms. For more details, see Supporting Data.

Results

DESI-MS lipid profiles from glioma tissue

DESI-MS imaging was performed on thirty-six human glioma samples including oligodendrogliomas, astrocytomas and oligoastrocytomas of different grades and varying tumor cell concentrations. A complete description of the samples used in this study, including information on glioma subtype, grade, recurrence, tumor cell concentration, EGFR copy number status, 1p/19q status, and p53 immunoreactivity is provided in Table S1. While analysis was performed in both the positive and negative ion mode, results are described using the data obtained in the negative ion mode, in which the most significant discrimination among lipid profiles was observed. Reproducibility was investigated by analyzing different tissue sections of the same sample on different days under the same experimental conditions (Fig. S1A-B, Supporting Information). The main lipid species observed in the examination of human glioma tissue in the mass range of *m/z* 200 to 1000 were saturated and unsaturated fatty acids (FA), glycerophosphoinositols (PI), glycerophosphoserines (PS), plasmenyl glycerophospho ethanolamines (plasmenyl-PE), and sulfatides (ST) (20). Lipid profiles from the samples of the three different glioma subtypes and of the samples of different grades within each glioma subtype were evaluated. Different lipid profiles were observed from astrocytoma samples of grades II, III, and IV (Fig. S2A-C). Grade II astrocytoma samples showed the presence of ST species, as well as PS and PI. Conversely, all grade IV astrocytomas analyzed consistently showed absence of sulfatide species, with high abundance of PS and PI species. Interestingly, grade IV astrocytoma, which displays very diverse cytomorphology on histologic sections (24), yielded reproducible DESI-MS lipid profiles in a range of samples with a lower total abundance of lipids than the low-grade astrocytomas.

The WHO recognizes two grades of oligodendroglial tumors, grade II for well-differentiated tumors, and grade III for anaplastic tumors. Representative lipid profiles are presented in Fig. S3A-B. Oligodendrioglioma is composed of neoplastic cells resembling oligodendroglia and characteristically harbors deletions in the 1p and 19q chromosomal arms. Oligoastrocytoma represents a mixed glial tumor that is composed of distinct neoplastic cells resembling both those found in oligodendroglioma and astrocytoma. The most abundant lipid species observed in the representative spectra of samples G41 (oligodendroglioma grade II) and G23 (oligodendroglioma grade III) are plasmenyl-PE, PS,

and PI. Free fatty acids such as palmitic acid FA(16:0), *m/z* 255.3, stearic acid FA(18:0), *m/z* 283.3 and arachidonic acid FA(20:4), *m/z* 303.2, and fatty acid dimers in the region of *m/z* 500 to *m/z* 650 were observed in both grades of oligodendrogliomas (16).

The most abundant lipid species observed in the mixed oligoastrocytoma grades II and III are the PS and PI (Fig. S4A-B), with some similarity to oligodendrogliomas. Sulfatides were present in grade III oligoastrocytomas, suggesting an astrocytoma content of the mixed tumor. Similar trends in the increase of relative abundance of PS(40:4), *m/z* 838.3 with increase of the oligodendroglioma grade are observed in the mixed oligoastrocytomas, likely representing the oligodendriogial character of this mixed glioma. Furthermore, grade II oligoastrocytoma presented higher relative intensities of plasmenyl-PEs and glycerophosphoglycerols PG, when compared to grade III oligoastrocytoma, a trend not as clearly observed for any of the other subtypes of gliomas.

A comparison of the lipid profiles from different subtypes of glioma samples with WHO grade III is shown in Fig. 1A-C. The lipid profile of a grade III astrocytoma contains lipid species of all PS, PI and ST classes, while the grade III oligodendroglioma shows a distinct profile of lipid species with PS(40:4) *m/z* 838.3, and PI(38:4) *m/z* 885.5 present at much higher relative abundances than observed in the pure astrocytoma. The grade III oligoastrocytoma sample presents a profile of PS and PI similar to the oligodendroglioma profile, with the presence of ST species at a lower relative abundance.

Morphological heterogeneity within tumor types can take many forms. One visually striking example of heterogeneous cellular elements are gemistocytic cells. On H&E stained sections these cells appear to have fat/plump, eccentrically placed nuclei and glassy cytoplasm. In our sample set, we had three cases with a distinct population of gemistocytic cells: a GBM (sample G46), a grade II oligodendroglioma (sample G49) and a grade III oligoastrocytoma (G45). Interestingly, these samples containing gemistocytic cells all showed a distinctive lipid profile with abundant signals for a set of fatty acids and fatty acid dimers. In the grade II oligodendrioglioma sample G49, we not only detected the phospholipid profile (*m/z* 700 – 900) characteristic of oligodendrogliomas (transitional between grade II and grade III) (Fig. 2A-D), but we also noted a very abundant signal of free fatty acid, specifically palmitic acid, *m/z* 255, oleic acid, *m/z* 281 and arachidonic acid, *m/z* 303, and fatty acid dimers in the region of *m/z* 500 to *m/z* 650. This characteristic profile was observed from all samples harboring gemistocytes, showing the ability of DESI-MS to distinguish the presence of this component in surgical specimens.

Mass spectrometry imaging

One of the advantages of imaging tissue sections by DESI-MS in comparison to profiling the mass/intensity distributions from tissue extracts is the preservation of morphologic features, providing means for visual differentiation of areas with heterogeneity and infiltration levels within the entire tissue section, and for building accurate reference systems. Negative ion mode DESI-MS ion images of sample G23, an oligodendroglioma grade III with 95% tumor cell concentration, are shown in Fig. S5A-H. A relatively homogeneous distribution of detected lipid species was observed in the ion images obtained for this sample, as seen in the ion images of the most abundant ions.

In contrast, sample G33, a glioblastoma with an overall 80% tumor cell concentration, demonstrates marked heterogeneity according to DESI-MS ion images (Fig. 3A-F). As before, the isomer assignments are not completely unambiguous even though tandem mass spectrometric data has been obtained on ions. Two regions with distinctive lipid profiles were observed from this section (Fig. 3G-H). Detailed histopathology evaluation of an H&E stained adjacent tissue section (Fig. 3I) revealed that the region delineated with blue is of

grade IV astrocytoma (GBM) with nearly 100% tumor cell concentration and focal vascular proliferation, while the region delineated with red is composed of mainly grey matter infiltrated by glioma cells, with lower tumor cell density (~30%). Indeed, the lipid profile detected in the pure glioblastoma region was consistent with the characteristic lipid profile of other glioblastoma samples, while a distinctly different lipid profile was detected in the region of infiltrated grey matter. Fig. 3J shows a plot of intensity of discriminating lipid species as a function of their location. The capability of DESI-MS imaging to clearly distinguish these two regions based on the lipid composition demonstrate its potential in detecting tumor margins and regions of higher and lower malignancy with an approximate spatial resolution of 200 μm. Another similar example is shown in Fig. S6A-F for sample G40, an oligodendroglioma grade II.

Statistical Analysis

While qualitative association of lipid profile constitution and spatial distribution with grade and subtype of gliomas can be generally observed from high-density specimens, a more suitable approach is to perform statistical evaluation of the entire data set. The high dimensionality of 2D imaging data together with visual alignment to optical imaging of tissue provides an opportunity to develop robust classification models with the potential to streamline surgical pathology.

Classification models were built to recognize glioma subtype and grade based on the WHO tumor classification system (22). A preliminary model was also built to assess tumor cell concentration in low, medium, and high density subsets based on the overall histopathology evaluation of the specimen. A list of the samples used to build the models is given in Table S2. All three classifiers had overall recognition capabilities > 99%, and cross validation > 97% (Table 1). Using the peak calculation criteria reported in the methods section, the software recognized 128 peaks for the subtype dataset, 123 peaks for the grade dataset, and 136 for the concentration dataset as being statistically significant between *m/z* 200- 1000. Classification models were built from these peak lists with an upper limit of 25 peaks to be used to distinguish classes (Table S3). Although chemical identification of the ions is not required for classification purposes, most of the lipid species selected by the classifier were identified based on collision-induced dissociation experiments (CID) tandem MS experiments and comparison with literature data (Table S4).

Discussion

This work demonstrates for the first time a comprehensive lipidomic based diagnostic approach for the classification of gliomas, the most common primary human brain tumor. Classification of DESI-MS imaging data demonstrated both high recognition capability and robust cross-validation. In addition, DESI MS imaging allowed discrimination of tumor from infiltrated brain hence delineating tumor margins. In all, the work provides a new modality to bridge neurosurgery and neuropathology and to help foster improved clinical decision-making (25).

In developing classifiers, the training sets used specimens demonstrating classic histologic features. Complex specimens resulting from recurrence were evaluated in the validation set. Despite the challenging nature of these test specimens, diagnostic information for the validation set was in clear agreement with the histopathology evaluation. This included 15 specimens evaluated for subtype, 17 specimens tested for grade, and 20 specimens for concentration. For example, specimen G41_0, which was diagnosed by histopathological evaluation as oligodendroglioma grade II/III with high tumor cell concentration (95%), was classified as 96% oligodendroglioma by the subtype classifier and 33% grade II and 67% grade III by the grade classifier. Specimen G41_1 was tested and correctly classified as high

tumor cell concentration (100%) by the concentration classifier. Sample G8, astrocytoma grade IV was tested solely in the subtype classifier, which correctly classified it as 98% astrocytoma.

Only ten discrepant results were noted for specimens of the validation set, which is noteworthy due to the heterogeneity and complexity of brain tumors. Note that discrepancy is defined very strictly as meaning not simultaneously satisfying all three criteria. A misassignment of concentration, or grade, or stage is interpreted as discrepant. Five of these were from the tumor cell concentration classifier. This classifier was built considering the overall concentration of the specimens, using limited regions of approximately 100 spectra to define the model. While these ROIs were selected to minimize background signal from the glass, the local tumor cell concentration was not taken into consideration, likewise for the ROIs tested for concentration from the validation set. For the grade classifier, three results from two different cases showed discrepancy with clinical diagnosis. G48 was diagnosed as an astrocytoma grade IV (GBM) with focal gliosarcoma, which is a GBM variant characterized by biphasic tissue pattern with alternating areas displaying glial and mesenchymal differentiation (22). The classifiers indicated a subtype distribution between the three different subtypes, and 90% of the tested spectra to be of grade II character. The current classifiers have not been trained to recognize this subtype of GBM, which has a high content of connective tissue. Classification of specimen G49 also resulted in a priori discrepancy with diagnosis. The histopathology evaluation of the specimen indicates an oligodendrioglioma grade II with very high concentration of gemistocytic cells. The classifiers recognize this specimen as a grade III astrocytoma with high tumor cell concentration, which would appear to reflect the highly gemistocytic area analyzed.

Specimen G20 was diagnosed as an oligoastrocytoma grade II, although a prior resection at an outside hospital was diagnosed as a diffuse astrocytoma. FISH results for evaluation of 1p19q deletion showed 1p deletion in 16/50 nuclei and 19q deletion in 4/50 nuclei, suggesting an oligodendroglial component to this tumor, but still do not explain the classification results as being 100% of oligodendrioglioma subtype. The histologic diagnosis of oligoastrocytoma is often challenging in the clinical setting, this glioma type is characterized by poor diagnostic concordance and reproducibility (26, 27). In an effort to dissect the heterogeneity in the oligoastrocytoma class, IHC was performed to evaluate the status of p53 (26) in addition to considering 1p19q status. The overall results are reported in Table S1, with 7/8 specimens tested to be positive for p53 expression. Fig. 4A-B shows the difference in p53 expression for the negative specimen G12 and for the positive specimen G21 (1p19q evaluation failed), indicating clearly the difference between the two specimens diagnosed as oligoastrocytomas. A strong nuclear staining for p53 often correlates with TP53 mutation and is more typical for low-grade astrocytomas, suggesting an astrocytic character to these tumors. The heterogeneity in this subtype likely explains some of the limitations of the subtype classifier in discriminating oligoastrocytomas from astrocytomas and oligodendriogliomas.

Since spatial information is retained and associated with the spectra throughout the classification process, results can be visualized as a class image using a color code corresponding to each of the classes of a given classifier and aligned to the optical image of an adjacent section. This allows to validate results with expert histopathology evaluation of the tissue, and could become a visualization mean of mass spectrometry based diagnosis. G26 is a very homogenous grade IV astrocytoma (GBM), which is clearly visible from the class imaging results (Fig. 5A), while G33 heterogeneity is clearly observed with the infiltrative region classified as a different tissue type with oligodendrioglioma character (Fig. 5B).

The utility of visualizing class images is shown in Fig. 6 for sample G40. This is an oligodendrogliomagrade II with tumor cells infiltrating white matter. The region of heterogeneity is further investigated by placing a transparent overlay of classification results on the optical image, revealing aggregates of tumor cells. This region appears as a weaving of low, medium, and high concentrations of tumor cells, and also presents with a potential region of progression to a higher grade. Tumor heterogeneity is common on histopathology evaluation of gliomas, but the operative criteria for prognostic and therapeutic decision-making is based on the presence of high-grade areas, even if present focally. DESI mass spectrometry analysis of surgical tissues has the potential to reconcile both by providing detailed diagnostic information in near real time to guide therapy.

Many of the PI, PS and ST species that were qualitatively observed to be different between subtypes of gliomas (Fig. 1A-C) were recognized by the subtype classifier. Additionally, some peaks not easily observed by visual inspection of the mass spectra, such as PS(40:5), m/z 836.2, were recognized by the classifier. While the identity of most of these species is still being investigated, a few are recognized as free fatty acids, such as arachidonic acid, m/z 303.2. The two most significant peaks recognized by the grade classifier were m/z 885.4, PI(18:0/20:4), and m/z 838.3, PS (18:0/22:4), which had also been qualitatively recognized as varying between different grades within each subtype, in terms of relative intensities (20).

This study validates the preliminary indications of discrimination between astrocytoma types by DESI imaging seen in a preliminary study. It also suggests that the analytical performance characteristics of the methodology are adequate to the challenge of reproducibility and information content to allow classification of tissue into the many sub-types represented by the various combinations of type, grade and concentration encountered in the brain. This ruggedness in performance together with the relative simplicity of the imaging methodology and especially the fact that the tissue is examined without prior chemical treatment makes the approach highly encouraging for development as an intraoperative procedure. We anticipate that the recent development of non-destructive solvent systems for DESI-MS imaging should enable even higher and more accurate correlation between MS lipidomic data and tissue morphology (28). The molecular information obtained by DESI-MS imaging analysis of glioma tissue can also provide means of understanding the biochemical processes occurring during malignancy. We anticipate that the metabolic variations being captured by DESI-MS imaging may contribute to a re-evaluation of the traditional classification systems in medicine.

Supplementary Material

Refer to Web version on PubMed Central for supplementary material.

Acknowledgments

References

1. Upadhyay UM, Golby AJ. Role of pre- and intraoperative imaging and neuronavigation in neurosurgery. Expert Rev Med Devices. 2008; 5:65–73. [PubMed: 18095898]

2. Kettenbach J, Kacher DF, Koskinen SK, Silverman SG, Nabavi A, Gering D, et al. Interventional and intraoperative magnetic resonance imaging. Annu Rev Biomed Eng. 2000; 2:661–90. [PubMed: 11701527]

3. Black PM, Alexander E 3rd, Martin C, Moriarty T, Nabavi A, Wong TZ, et al. Craniotomy for tumor treatment in an intraoperative magnetic resonance imaging unit. Neurosurgery. 1999; 45:423–31. discussion 31-33. [PubMed: 10493363]

4. Black PM, Moriarty T, Alexander E 3rd, Stieg P, Woodard EJ, Gleason PL, et al. Development and implementation of intraoperative magnetic resonance imaging and its neurosurgical applications. Neurosurgery. 1997; 41:831–42. discussion 42-5. [PubMed: 9316044]

5. Jolesz FA, Nabavi A, Kikinis R. Integration of interventional MRI with computer-assisted surgery. J Magn Reson Imaging. 2001; 13:69–77. [PubMed: 11169806]

6. Louis DN, Ohgaki H, Wiestler OD, Cavenee WK, Burger PC, Jouvet A, et al. The 2007 WHO classification of tumours of the central nervous system. Acta Neuropathol. 2007; 114:97–109. [PubMed: 17618441]

7. MacConaill LE, Campbell CD, Kehoe SM, Bass AJ, Hatton C, Niu L, et al. Profiling critical cancer gene mutations in clinical tumor samples. PLoS ONE. 2009; 4:e7887. [PubMed: 19924296]

8. Schwartz SA, Weil RJ, Thompson RC, Shyr Y, Moore JH, Toms SA, et al. Proteomic-based prognosis of brain tumor patients using direct-tissue matrix-assisted laser desorption ionization mass spectrometry. Cancer Research. 2005; 65:7674–81. [PubMed: 16140934]

9. Cowart LA. Sphingolipids: players in the pathology of metabolic disease. Trends in Endocrinology and Metabolism. 2009; 20:34–42. [PubMed: 19008117]

10. Podo F, Sardanelli F, Iorio E, Canese R, Carpinelli G, Fausto A, et al. Abnormal choline phospholipid metabolism in breast and ovary cancer: Molecular bases for noninvasive imaging approaches. Curr Med Imaging Rev. 2007; 3:123–37.

11. Sakai K, Okuyama H, Yura J, Takeyama H, Shinagawa N, Tsuruga N, et al. Composition and turnover of phospholipids and neutral lipids in human breast cancer and reference tissues. Carcinogenesis. 1992; 13:579–84. [PubMed: 1576710]

12. Alberici RM, Simas RC, Sanvido GB, Romao W, Lalli PM, Benassi M, et al. Ambient mass spectrometry: bringing MS into the "real world". Anal Bioanal Chem. 2010; 398:265–94. [PubMed: 20521143]

13. Harris GA, Galhena AS, Fernandez FM. Ambient Sampling/Ionization Mass Spectrometry: Applications and Current Trends. Analytical Chemistry. 2011; 83:4508–38. [PubMed: 21495690]

14. Eberlin LS, Ferreira CR, Dill AL, Ifa DR, Cooks RG. Desorption Electrospray Ionization Mass Spectrometry for Lipid Characterization and Biological Tissue Imaging. BBA-Mol Cell Biol L. 201110.1016/j.bbalip.2011.05.006

15. Wiseman JM, Ifa DR, Venter A, Cooks RG. Ambient molecular imaging by desorption electrospray ionization mass spectrometry. Nat Protoc. 2008; 3:517–24. [PubMed: 18323820]

16. Dill A, Eberlin LS, Costa AB, Zheng C, Ifa DR, Cheng L, et al. Multivariate Statistical Identification of Human Bladder Carcinomas using Ambient Ionization Imaging Mass Spectrometry. Chem -Eur J. 2011; 17:2897–902. [PubMed: 21284043]

17. Dill AL, Eberlin LS, Zheng C, Costa AB, Ifa DR, Cheng LA, et al. Multivariate statistical differentiation of renal cell carcinomas based on lipidomic analysis by ambient ionization imaging mass spectrometry. Anal Bioanal Chem. 2010; 398:2969–78. [PubMed: 20953777]

18. Eberlin LS, Dill AL, Costa AB, Ifa DR, Cheng L, Masterson T, et al. Cholesterol Sulfate Imaging in Human Prostate Cancer Tissue by Desorption Electrospray Ionization Mass Spectrometry. Analytical Chemistry. 2010; 82:3430–4. [PubMed: 20373810]

19. Masterson TA, Dill AL, Eberlin LS, Mattarozzi M, Cheng L, Koch MO, et al. Distinctive Glycerophospholipid Profiles of Human Seminoma and Adjacent Normal Tissues by Desorption Electrospray Ionization Imaging Mass Spectrometry. J Am Soc Mass Spectrom. 2010 in press.

20. Eberlin LS, Dill AL, Golby AJ, Ligon KL, Wiseman JM, Cooks RG, et al. Discrimination of Human Astrocytoma Subtypes by Lipid Analysis Using Desorption Electrospray Ionization Imaging Mass Spectrometry. Angew Chem Int Ed. 2010; 49:5953–6.

21. Stoeckli, M. msimaging. 2003. [cited; Available from: http://maldi-msi.org/

22. Louis, DN.; Ohgaki, H.; Wiestler, OD.; Cavenee, WK. WHO Classification of Tumors of the Central Nervous System. 4th. Lyon: WHO Press; 2007.

23. Natterer, M.; Neumann, S. GNU Image Manipulation Program. 2001. [cited; Available from: www.gimp.org

24. Bonavia R, Inda MD, Cavenee WK, Furnari FB. Heterogeneity Maintenance in Glioblastoma: A Social Network. Cancer Research. 2011; 71:4055–60. [PubMed: 21628493]

25. Agar NY, Golby AJ, Ligon KL, Norton I, Mohan V, Wiseman JM, et al. Development of stereotactic mass spectrometry for brain tumor surgery. Neurosurgery. 2011; 68:280–89. discussion 90. [PubMed: 21135749]

26. Gupta M, Djalilvand A, Brat DJ. Clarifying the diffuse gliomas: an update on the morphologic features and markers that discriminate oligodendroglioma from astrocytoma. Am J Clin Pathol. 2005; 124:755–68. [PubMed: 16203285]

27. Ueki K, Nishikawa R, Nakazato Y, Hirose T, Hirato J, Funada N, et al. Correlation of histology and molecular genetic analysis of 1p, 19q, 10q, TP53, EGFR, CDK4, and CDKN2A in 91 astrocytic and oligodendroglial tumors. Clin Cancer Res. 2002; 8:196–201. [PubMed: 11801559]

28. Eberlin LS, Ferreira CR, Dill AL, Ifa DR, Cheng L, Cooks RG. Nondestructive, histologically compatible tissue imaging by desorption electrospray ionization mass spectrometry. Chembiochem. 2011; 12:2129–32. [PubMed: 21793152]
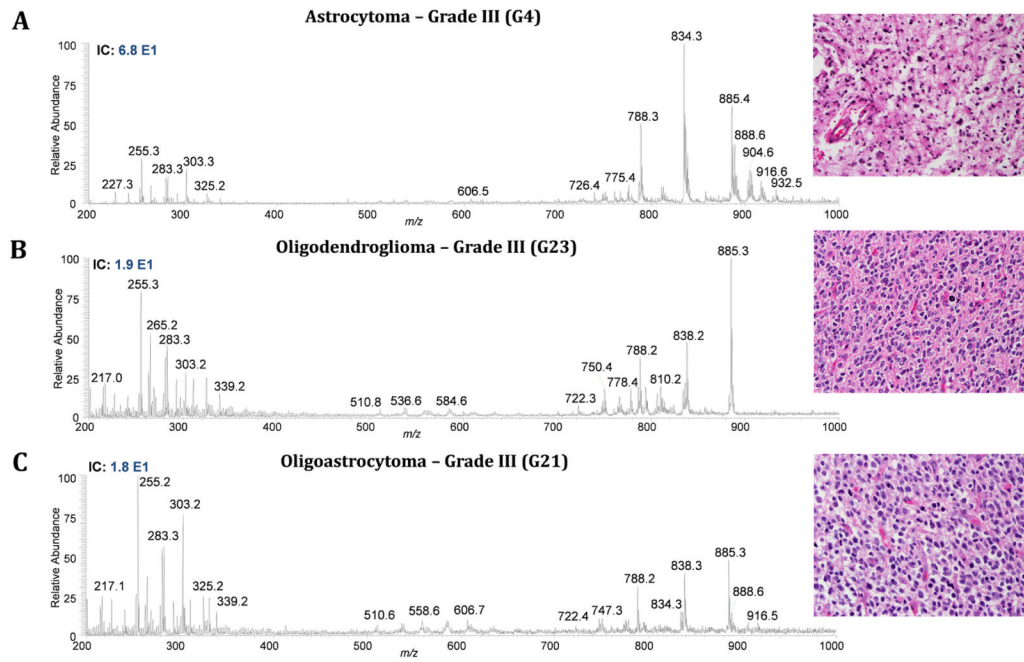
Figure 1.
Discrimination between subtypes of grade III gliomas is achieved through lipid profiles detected by DESI-MS. Representative negative ion mode mass spectra from different grade III subtypes of human gliomas, (**A**) anaplastic astrocytoma, (**B**) anaplastic oligodendroglioma and (**C**) anaplastic oligoastrocytoma. Insets show bright field optical images (400×) of the corresponding diagnostic permanent H&E section.
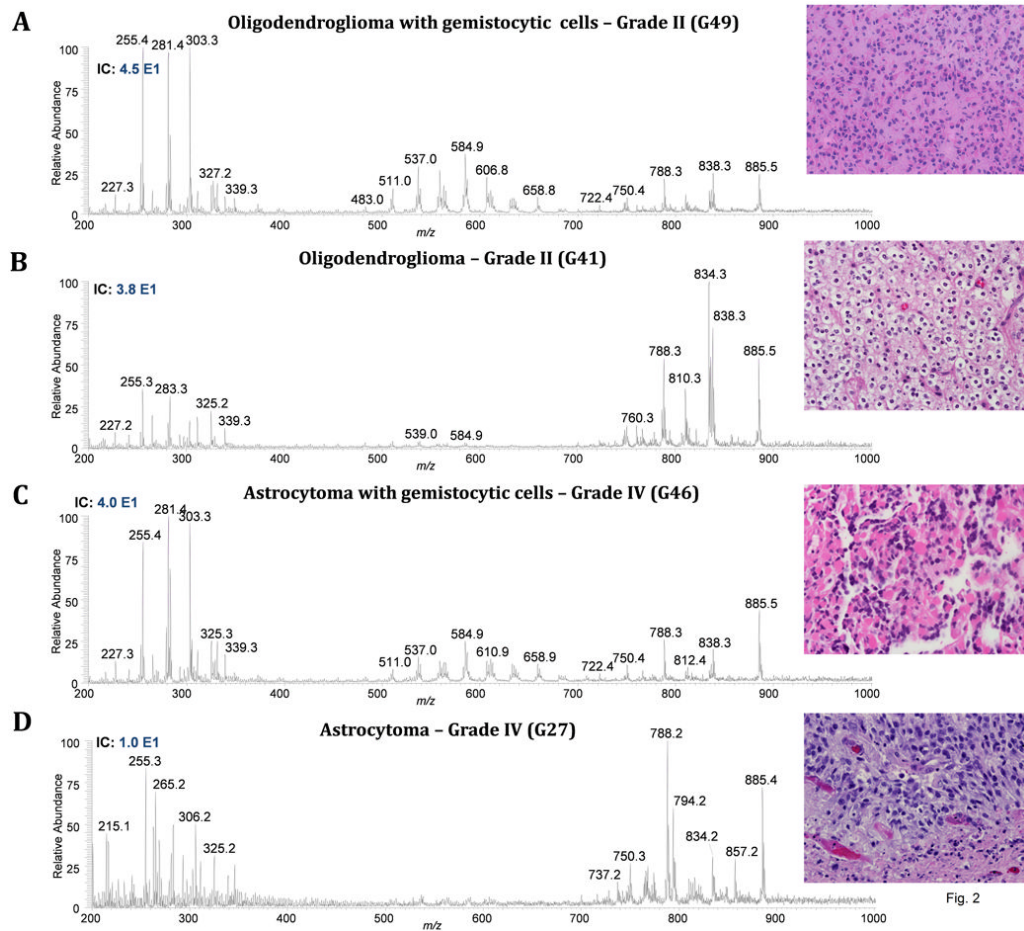
Figure 2.
Distinctive lipid profiles with high abundance of fatty acids and dimers are detected for samples with gemistocytic cells. DESI-MS negative ion mode mass spectra of (**A**) sample G49, oligodendroglioma grade II with gemistocytes; (**B**) sample G41, oligodendroglioma grade II; (**C**) sample G46, astrocytoma grade IV with gemistocytes and (**D**) sample G27, astrocytoma grade IV. Insets show the magnified bright field optical images of the corresponding diagnostic permanent H&E section, with the exception of (**A**) being from a frozen section.
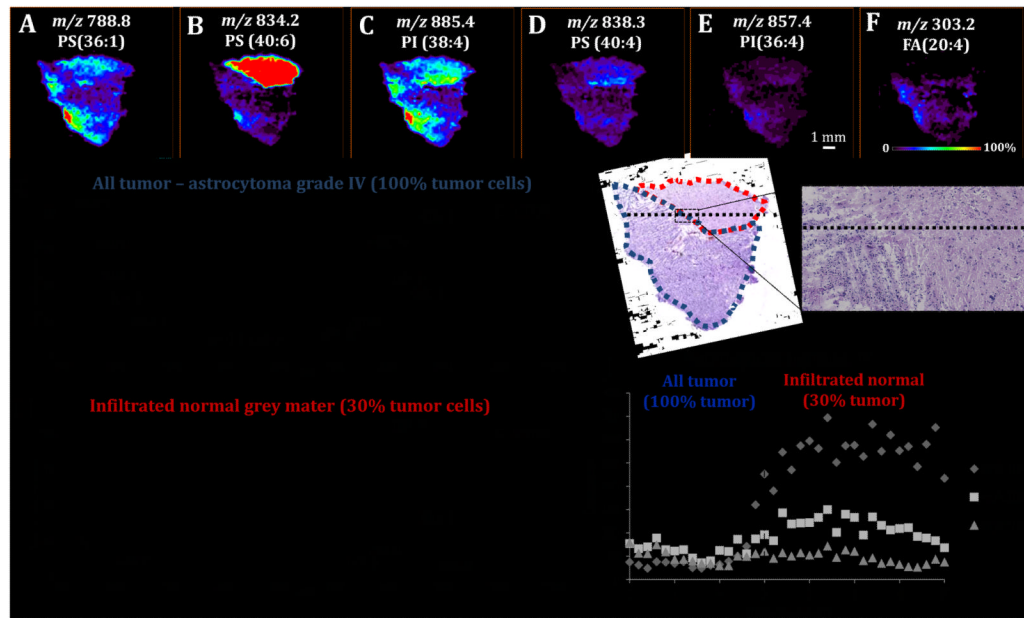
Figure 3.
Tumor heterogeneity and infiltration is assessed by DESI-MS imaging. Negative ion mode DESI-MS ion images of glioblastoma G33showing the distribution of (**A**) *m/z* 788.8, PS(36:1); (**B**) *m/z* 834.2, PS(40:6); (**C**) *m/z* 885.4, PI(38:4); (**D**) *m/z* 838.3, PS(40:4); (**E**) *m/z* 857.3, PI(36:4) and (**F**) *m/z* 303.3, FA(20:4). The color scale used in ion images is shown in (**F**), which is normalized to the most intense (100% relative intensity, red color) peak in the mass spectra. Mass spectra are shown from regions delineated with (**G**) blue and (**H**) dotted lines, diagnosed as a region of 100% tumor cell concentration and infiltrated grey matter (30% tumor cell), respectively. Optical image of the H&E stained adjacent section is shown in (**I**), showing heterogeneous regions and the border between those magnified. In (**J**), a plot of the total abundance of the ions *m/z* 834.2, *m/z* 885.4 and *m/z* 788.8 by the distance (mm) throughout the dotted black line marked in H&E stained optical image of (**I**) is shown.

A G12 – OA grade II

p53 weak
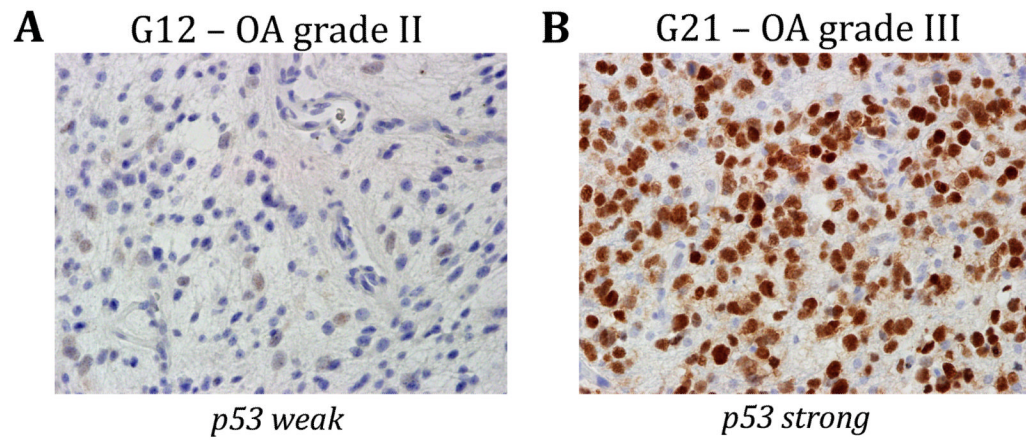
B G21 – OA grade III

p53 strong

Figure 4.
p53 expression in two oligoastrocytoma samples. (**A**) specimen G12, OA grade II (negative) and (**B**) specimen G21, OA grade III (positive). Different expression of p53 indicates difference between the two specimens diagnosed as oligoastrocytomas.
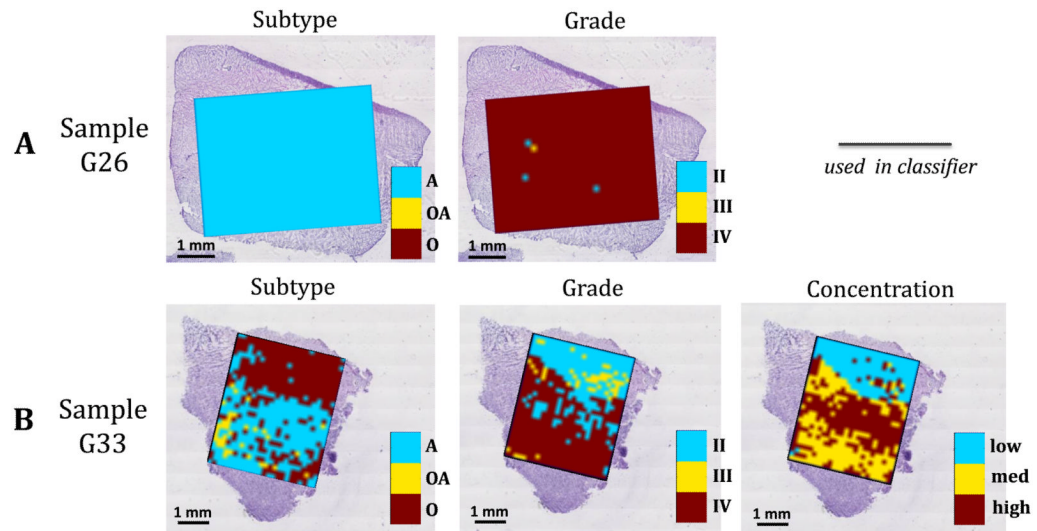
Figure 5.
Classification results can be visualized as a class image using a color code corresponding to each of class and registered to the optical image of an adjacent section. Subtype, grade, and concentration classification for (**A**) Sample G33, (heterogeneous) and (**B**) Sample G26 (homogenous).
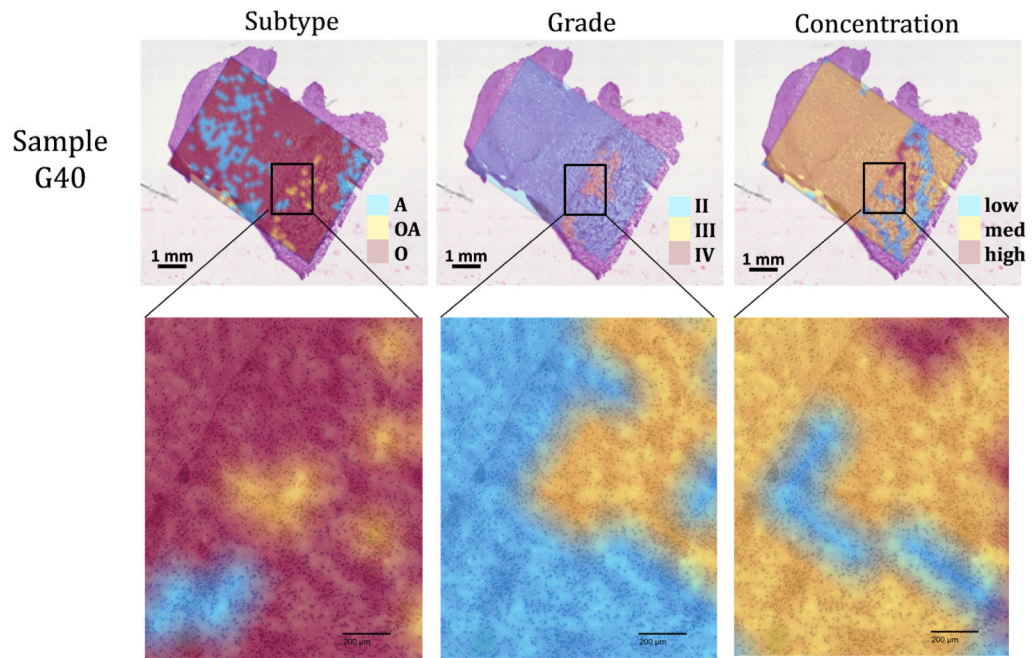
Figure 6.
Transparent classification results overlay onto optical imaging of an H&E stain of specimen G40. The tissue section is recognized has an oligodendrioglioma grade II with a region of heterogeneity with clumps of tumor, as shown in the magnification of the region of interest. The scale bar of 200 μm also represents the defined diameter of the DESI spray used in the imaging experiments, dictating the spatial resolution of corresponding images.

Table 1

Classification results for subtype, grade and concentration classifiers applied to validation set of samples.

	Subtype	Grade	Concentration
		%	
Overall Recognition Capability	99.3	99.7	99.0
Cross Validation	97.9	99.2	97.5

		Subtype			Grade			Concentration		
						%				
Name	WHO Diagnosis	A	OA	O	II	III	IV	low	med	high
G6	A-IV; high	100	0	0				1	84	15
G8	A-IV; recurrent A-IV	98	0	2						
*G26	A-IV; recurrent OA-III	100	0	0	0	0	99			
G28	A-IV				0	8	92			
G31	A-IV; recurrent A-III/GBM				0	0	100			
G32	A-IV; recurrent A-IV, High	94	0	6	16	33	51	48	9	43
* G33	A-IV; high	45	5	49	21	36	43	1	1	98
G48	A-IV; focal gliosarcoma	37	14	49	90	10	0	44	23	33
G35	A-IV; high							19	20	61
G30	A-IV-O; recurrent; high	100	0	0	0	5	95	4	14	82
G29	A-IV-O; recurrent OA-III	69	0	31	32	36	32	77	17	6
G5	A-IV-O; high (80%)	42	32	26				12	84	4
G47_0	A-IV-O; recurrent O-II	43	17	40	65	0	35	1	0	99
G47_1	A-IV-O; recurrent O-II	55	0	45	100	0	0	47	53	0
G10	O-II, med				100	0	0	12	87	1
* G40	O-II, infiltrated	20	3	78	94	6	0	12	85	3
G42_0	O-II focal O-III; High							1	10	89
G42_1	O-II focal O-III; High				82	18	0	0	3	97
G43_0	O-II focal O-III; High							14	21	66

	Subtype			Grade			Concentration		
				%					
G43_1 O-II focal O-III; High							9	15	76
G49 O-II; gemistocytes, High	**98**	**1**	**1**	**2**	**91**	**7**	**0**	**0**	**100**
G41_0 O-II/III; recurrent O-II, High	3	2	96	33	67	0			
G41_1 O-II/III; recurrent O-II, High							0	0	100
G20 OA-II; residual A-II; med (30%)	*0*	*0*	*100*	**90**	**5**	**5**	**89**	**2**	**9**
G13 OA-II-III; recurrent OA-II-III				2	98	0			
G45 OA-III; residual OA-III, High							*0*	*97*	*3*

Astrocytoma (A), Oligoastrocytoma (OA), Oligodendroglioma (O)

Grey areas correspond to specimens used in a corresponding training set; italicized results are in apparent disagreement with diagnosis and further discussed; boldface type results highlight validation samples not used in any of the training sets.

*
G33 Tested on a region of 696 spectra for subtype, and on region of 192 spectra for grade; G26 tested on region of 744 spectra for grade; G40 tested on a region of 900 spectra.

Cross validation (leave-out 20%/10 iterations)